Supporting Information: Calculation of Ligand Dissociation Energies in Large Transition-Metal Complexes

Tamara Husch, Leon Freitag, and Markus Reiher*

ETH Zürich, Laboratorium für Physikalische Chemie,
Vladimir-Prelog-Weg 2, 8093 Zürich, Switzerland.

March 20, 2018

1 Orbital Entanglement and Active Space Selection for Multi-Configurational Calculations

The active orbital spaces for multi-reference calculations were selected with an automated selection protocol developed in our group.[1–3] The selection is based on orbital entanglement measures, namely single-orbital entropy $s(1)_i$ and mutual information I_{ij}. For more information on these concepts, we refer to Refs. 4, 5. The active spaces of the dissociated and the undissociated species must match each other to ensure size consistency. When the active space is selected for the dissociated and for the undissociated species independently, this is not guaranteed. Consequently, a union of the automatedly selected orbitals for the dissociated and for the undissociated species was applied as the final active orbital space as recommended in Ref. 1. The structure of the dissociated complex was generated by separating the two fragments by 10 Å within one structure file.

The orbital entanglement measures were determined from DMRG configuration interaction (DMRG-CI) wave functions. The active spaces for the DMRG-CI calculations range from 34 to 58 orbitals (Table 1) and comprise

*corresponding author: markus.reiher@phys.chem.ethz.ch.

at least the π system, the d orbitals of the metal, and the second d shells. The number of renormalized block states m was fixed at 512 for all DMRG-CI calculations. This m value usually suffices[1] to obtain a qualitatively correct orbital entanglement picture and a potential insufficiency could be detected by comparison with the final fully-converged DMRG results.

Most of the species involved in reactions in the WCCR10 set exhibit a $Z_{s(1)} < 0.20$ which indicates single-configurational character. Multi-reference calculations are generally not required to obtain accurate electronic energies for species with single-configurational character. Nevertheless, we were interested in a comparison of the results obtained with multi-reference and single-reference perturbation theories, and hence, needed to choose active orbital spaces for all species. Unfortunately, the largest single-orbital entropy $s(1)_{\max}$, and hence, the spread between the individual $s(1)_i$ values are small for species with a small $Z_{s(1)}$. Consequently, it is difficult to differentiate between orbital sets with similar $s(1)_i$ values, and hence, a fully automated orbital selection requires a well-converged DMRG-CI calculation. Such calculations may not be feasible for individual cases (and are usually not required because one is not interested in choosing active orbital spaces for single-configurational molecules) and we carried out small manual adjustments to the active orbital spaces which are given for each individual reaction.

The orbital basis for the DMRG-CI calculations was obtained from a smaller CASSCF calculation with metal d orbitals and bonding–antibonding linear combinations with the energetically close valence orbitals of the ligands (Table 1). We chose a smaller basis set for the DMRG-CI calculations than for the final CASSCF or DMRG-SCF calculations to avoid including Rydberg orbitals. This small basis set consists of a valence double-zeta polarised ANO-RCC-VDZP basis set for all metal atoms and a minimal basis ANO-RCC-MB basis set for all other atoms.

Table 1: Active spaces for (a) CASSCF and (b) DMRG-CI. The CASSCF calculations were carried out to obtain the final orbital basis for the DMRG-CI calculations. The calculations may be denoted as DMRG[512](a)#CAS(b)-SCF in the notation of Ref. 1. .)

Reaction	Undissociated		Dissociated	
	(a)	(b)	(a)	(b)
1	(10,9)	(38,37)	(10,9)	(54,58)
2	(10,10)	(34,34)	(10,10)	(34,34)
3	(10,10)	(34,34)	(10,10)	(34,34)
4	(10,8)	(36,36)	(10,8)	(36,36)
5	(14,14)	(50,56)	(14,14)	(50,58)
6	(13,13)	(56,55)	(13,13)	(56,60)
7	(12,12)	(54,57)	(14,14)	(54,58)
8	(12,12)	(52,55)	(12,12)	(54,54)
9	(10,10)	(36,40)	(10,10)	(36,37)
10	(10,10)	(40,43)	(10,10)	(40,34)

Reaction 1

The entanglement diagrams and the automatedly selected active orbital spaces for the undissociated and dissociated complexes in reaction 1 are shown in Figure 1a and 1b. An active space of 10 electrons in 10 orbitals (CAS(10,10)) is determined for the undissociated complex. This active orbital space consists of one d orbital, four π orbitals, and five π^* orbitals. The orbital optimization yields a bonding–antibonding linear combination of the selected d orbital with neighboring σ orbitals and four π and π^* orbital pairs. The active orbital space for the dissociated complex features only 9 π and π^* orbitals. One can see that the π^* orbital located on the ligand bridge (orbital 32, see Figure 1b) does not have a corresponding π orbital selected. This π orbital was manually added to the active orbital space. The final active space for reaction 1 is the union of the two active spaces for the undissociated and the dissociated complex, resulting in 12 electrons in 12 active orbitals (CAS(12,12), see Figure 2).

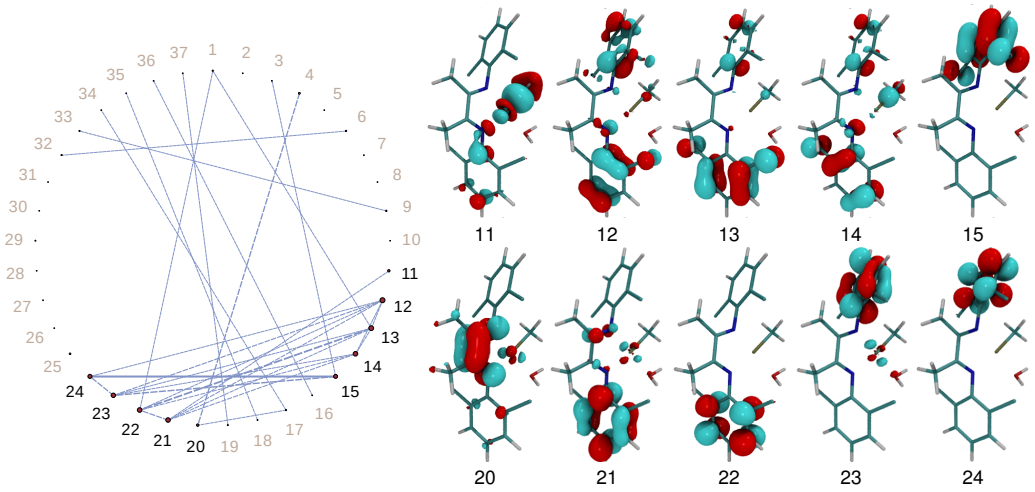

(a) Undissociated complex

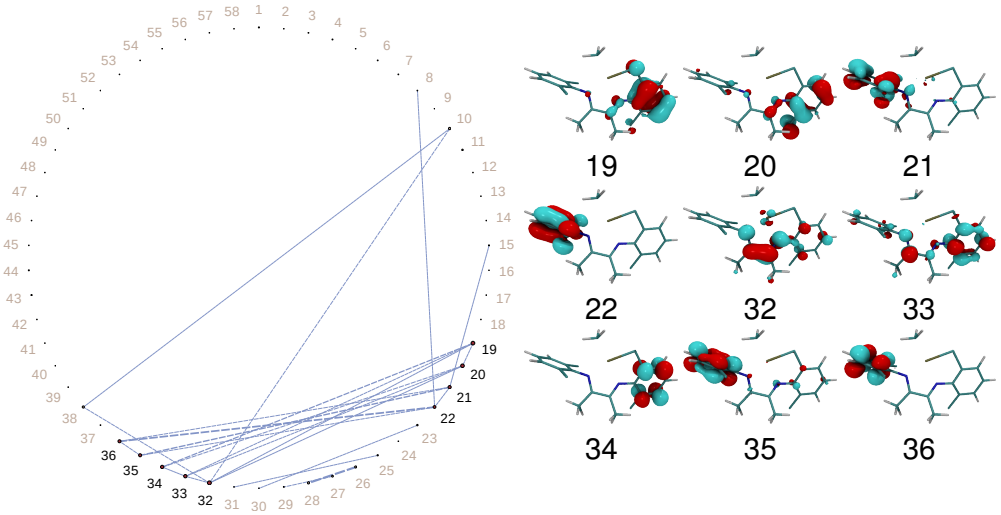

(b) Dissociated complex

Figure 1: Entanglement diagrams calculated from DMRG-CI wave functions for the undissociated (a) and dissociated (b) complex of reaction 1. The area of the red circle is proportional to the single-orbital entropy $s(1)_i$, the blue lines connecting the orbitals show their mutual information value I_{ij}. Solid lines denote I_{ij} values of at least 0.1, dashed lines I_{ij} values of at least 0.01. The automatedly selected orbitals are depicted around the circle and highlighted by black numbers.

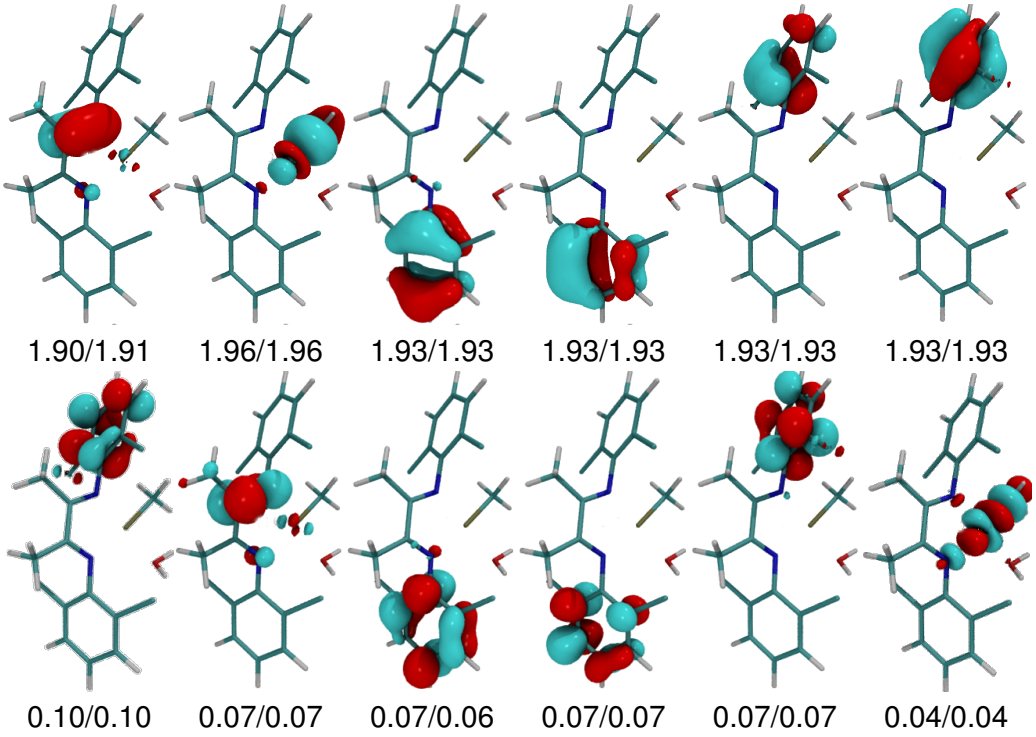

Figure 2: The final CAS(12,12) selected for reaction 1 with natural orbital occupation numbers (for the undissociated/dissociated complex, respectively).

Reactions 2 and 3

Reactions 2 and 3 feature the same undissociated complex and will be considered together. For the undissociated complex, 33 out of 34 orbitals are selected by the active space selection protocol which is, however, too large for a CASPT2 calculation. We manually chose a CAS(8,8) consisting of 4 π and π^* orbital pairs to be able to proceed with multi-reference perturbation theory calculations. The undissociated complex and the dissociated ones are a clear single-configurational cases as indicated by the $Z_{s(1)}$ measure which is below 0.10. Consequently, a CASPT2 calculation with this active space yields dissociation energies which only differ by 4.0 kJ mol^{-1} from single-configurational MP2 calculation with the same basis set.

Reaction 4

The entanglement diagrams and the automatedly selected active orbital spaces for the undissociated and for the dissociated complexes in reaction 4 are shown in Figure 3 and 4. Eleven active orbitals are selected for the undisso-

ciated complex: three π, two π^* orbitals, and a set of Ru d orbitals, including one bonding–antibonding linear combination with the neighboring σ orbitals. This active space is unbalanced because one of the three π orbitals is missing a corresponding π^* orbital. This π orbital is substituted for a metal $4p$ orbital during orbital optimization. The latter has an occupation number very close to 2 (1.997), and hence, may be omitted which results in a CAS(10,10) (see Figure 5). Two orbitals are automatedly selected for the dissociated complex. These two orbitals are already included in the CAS(10,10) of the undissociated complex, and hence, this CAS is employed as the final CAS for both complexes.

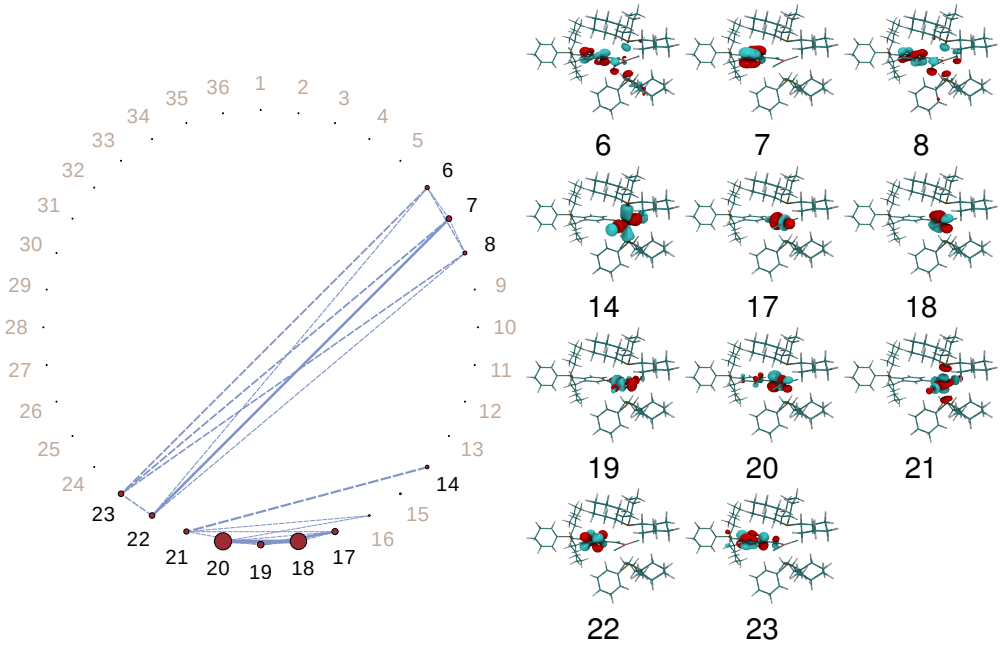

Figure 3: Entanglement diagrams calculated from DMRG-CI wave functions for the undissociated complex of reaction 4. The area of the red circle is proportional to the single-orbital entropy $s(1)_i$, the blue lines connecting the orbitals show their mutual information value I_{ij}. Solid lines denote I_{ij} values of at least 0.1, dashed lines I_{ij} values of at least 0.01. The automatedly selected orbitals are depicted around the circle and highlighted by black numbers.

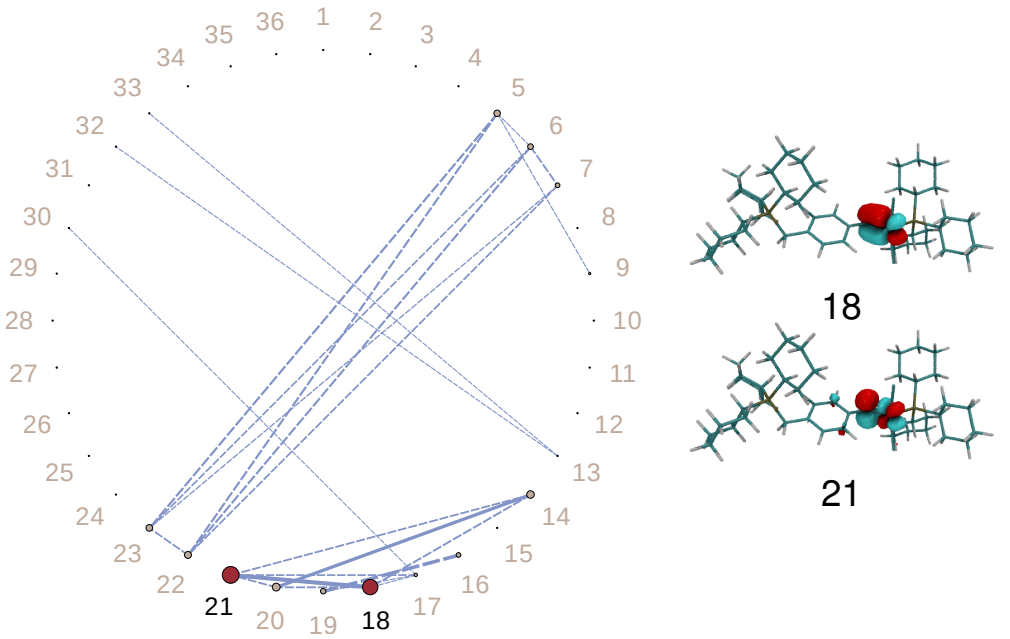

Figure 4: Entanglement diagrams calculated from DMRG-CI wave functions for the dissociated complex of reaction 4. The area of the red circle is proportional to the single-orbital entropy $s(1)_i$, the blue lines connecting the orbitals show their mutual information value I_{ij}. Solid lines denote I_{ij} values of at least 0.1, dashed lines I_{ij} values of at least 0.01. The automatedly selected orbitals are depicted around the circle and highlighted by black numbers.

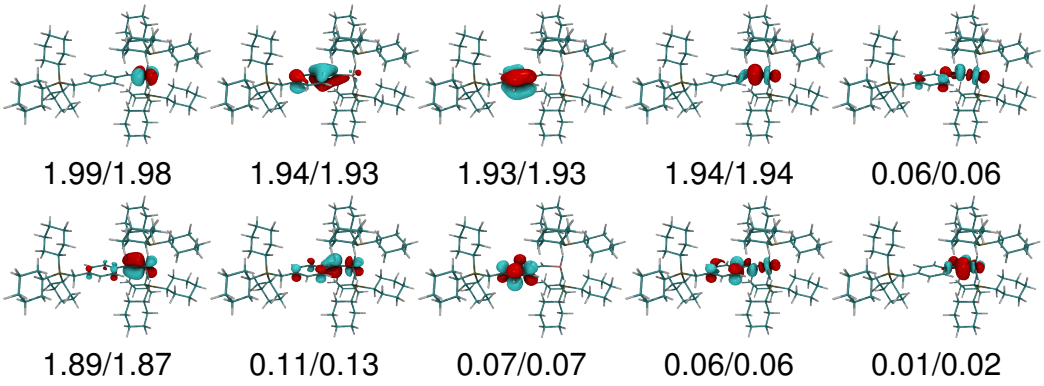

Figure 5: The final CAS(10,10) selected for reaction 4 with natural orbital occupation numbers (for the undissociated/dissociated complex, respectively).

Reaction 5

The entanglement diagram and the automatedly selected active orbital space (CAS(6,5)) for the undissociated complex of reaction 5 are shown in Fig-

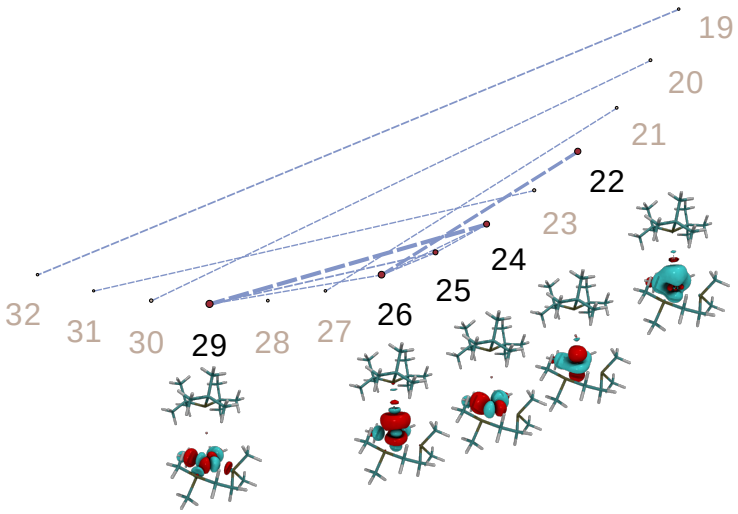

(a) Entanglement diagram for the undissociated complex

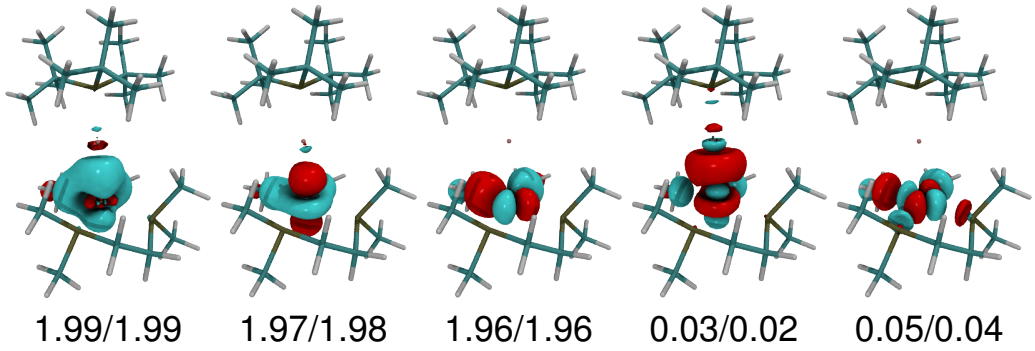

(b) Final CAS(6,5)

Figure 6: (a) Entanglement diagram calculated from DMRG-CI wave functions for the undissociated complex of the reaction 5. The area of the red circle is proportional to the single-orbital entropy $s(1)_i$, the blue lines connecting the orbitals show their mutual information value I_{ij}. Solid lines denote I_{ij} values of at least 0.1, dashed lines I_{ij} values of at least 0.01. The automatedly selected orbitals are depicted around the circle and highlighted by black numbers. (b) The final CAS selected with natural orbital occupation numbers (for the undissociated/dissociated complex, respectively).

ure 6a. This active orbital space includes a selection of Pt d orbitals and their linear combinations with neighboring σ orbitals. The CAS(6,5) determined for the undissociated complex was chosen as the final CAS for this reaction (see Figure 6b).

Reactions 6, 7, and 8

The undissociated complexes of reaction 6, 7, and 8 are isoleptic coinage metal complexes. All three metal centers (reaction 6, Au; reaction 7, Cu; reaction 8, Ag) have a d^{10} electronic configuration which typically points towards a low multi-configurational character. Figure 7 shows the entanglement diagram and the twelve automatedly selected orbitals for the undissociated complex of reaction 8. Due to the similarity of the reactions, we aim for a consistent active space for all three of them. For all (dissociated and undissociated) complexes in reactions 6, 7, and 8, the selected orbitals are a subset of these twelve orbitals. Hence, we chose the CAS(12,12) for all three reactions (see Figure 8).

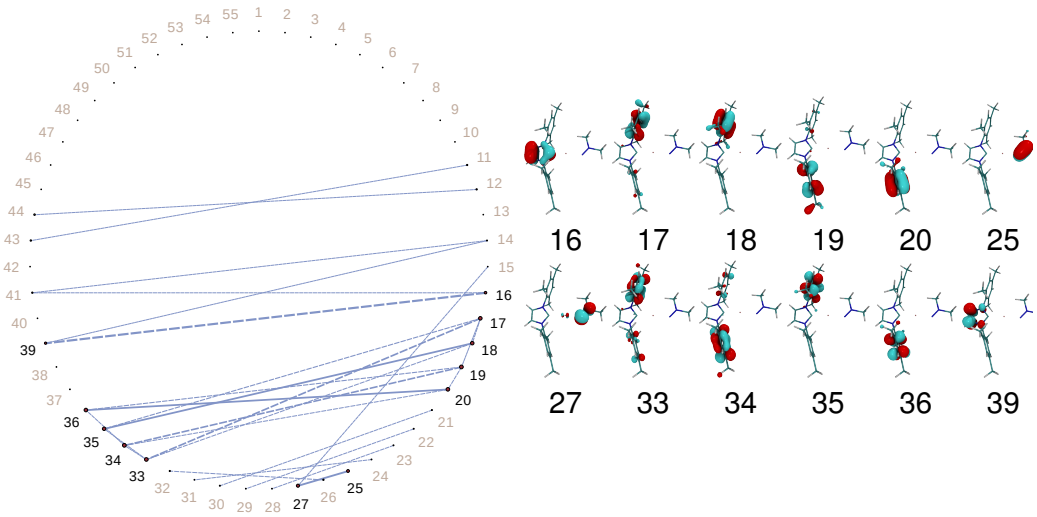

Figure 7: Entanglement diagram calculated from DMRG-CI wave functions for the undissociated complex of the reaction 8. The area of the red circle is proportional to the single-orbital entropy $s(1)_i$, the blue lines connecting the orbitals show their mutual information value I_{ij}. Solid lines denote I_{ij} values of at least 0.1, dashed lines I_{ij} values of at least 0.01. The automatedly selected orbitals are depicted around the circle and highlighted by black numbers.

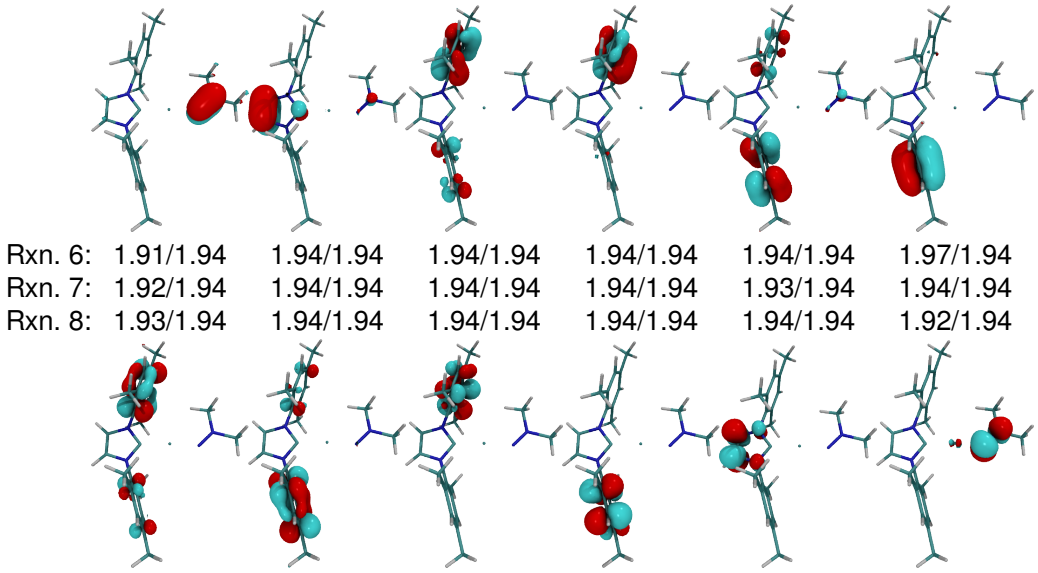

Figure 8: The final CAS(12,12) selected for reactions 6, 7, and 8 with natural orbital occupation numbers (for the undissociated/dissociated complex, respectively).

Reaction 9

An η^2 bond is cleaved in reaction 9. For such a reaction, one would expect an interaction of the metal d orbitals with the π^* orbitals of the phenyl group which points towards static correlation in this bond. Four orbitals are automatedly selected for the undissociated complex (15, 17, 19, and 21; see Figure 9a). This selection does not include all orbitals which one would expect to be relevant for the metal-ligand bond. Therefore, an active space corresponding to a second plateau in the $s(1)$ threshold diagram was selected (see Figure 11). This active space corresponds to 14 electrons in 14 orbitals and is displayed in Figure 10. Only one orbital is automatedly selected for the dissociated complex (10 in Figure 9b). An analogous plateau with 13 orbitals was, however, identified in the $s(1)$ threshold diagram. The final active space is again the union of the two active spaces which in this case comprises the 14 orbitals identified for the undissociated complex. $Z_{s(1)}$ is not defined when the number of orbitals does not equal the number of electrons[6] which is the case when one orbital is selected. Hence, the $Z_{s(1)}$ value in Table 1 of the main paper has been evaluated with the final active space.

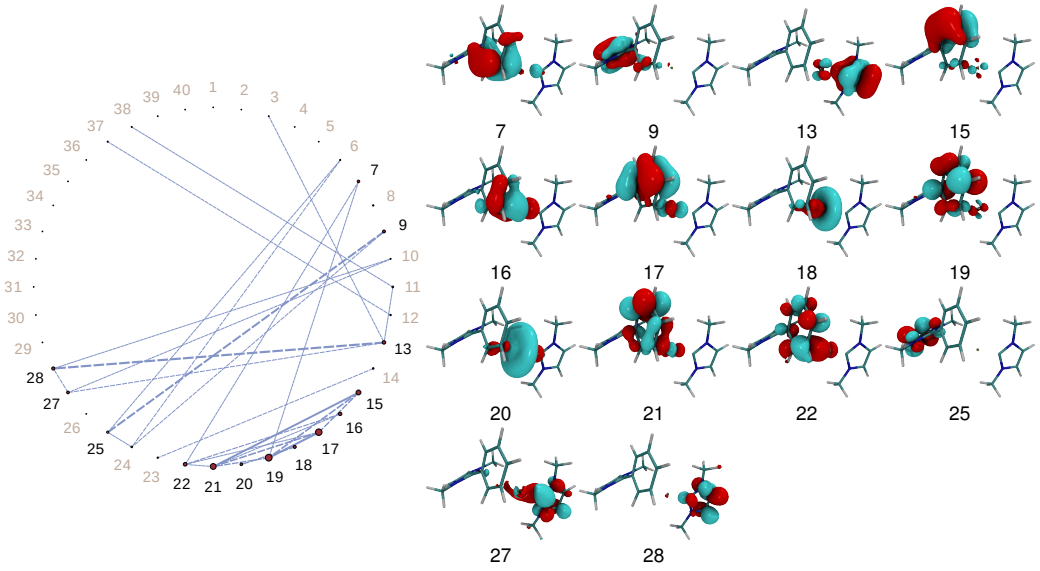

(a) Undissociated complex

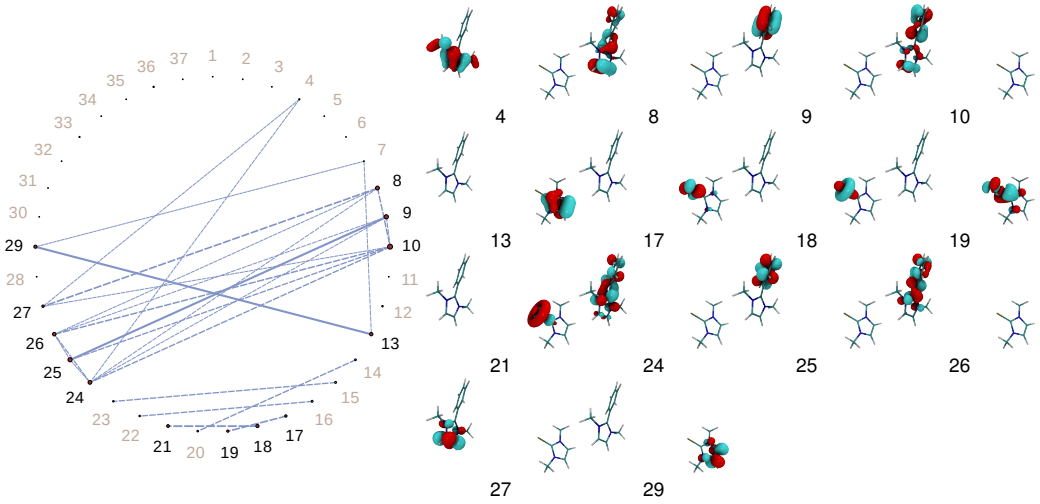

(b) Dissociated complex

Figure 9: Entanglement diagrams calculated from DMRG-CI wave functions for the undissociated (a) and dissociated (b) complex of reaction 9. The area of the red circle is proportional to the single-orbital entropy $s(1)_i$, the blue lines connecting the orbitals show their mutual information value I_{ij}. Solid lines denote I_{ij} values of at least 0.1, dashed lines I_{ij} values of at least 0.01. The automatedly selected orbitals are depicted around the circle and highlighted by black numbers.

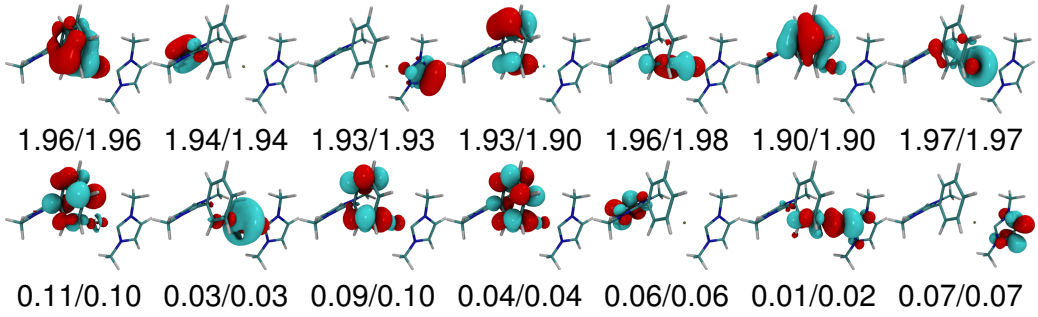

Figure 10: The final CAS(14,14) selected for reaction 9 with natural orbital occupation numbers (for the undissociated/dissociated complex, respectively).

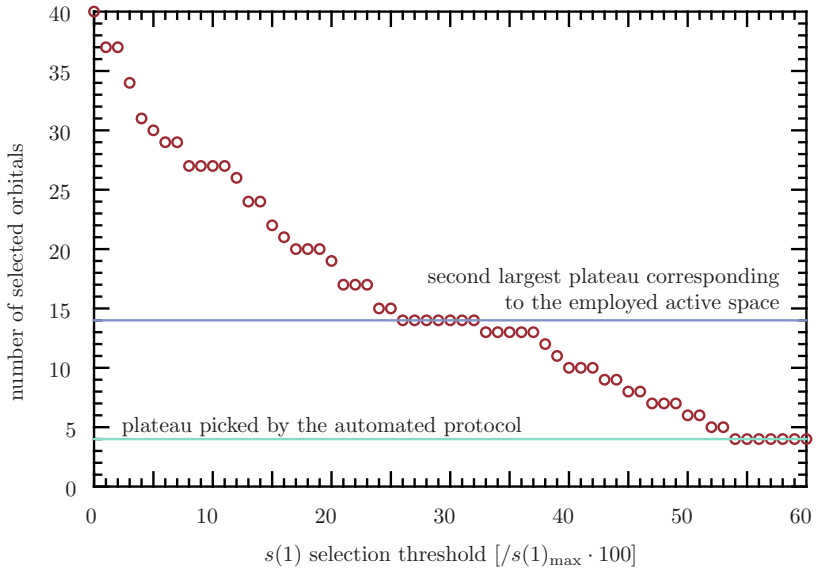

Figure 11: Number of selected orbitals depending on the selection threshold of $s(1)$ in percent of the largest $s(1)$ value. The automated selection picks the largest plateau with 4 orbitals (highlighted in green) which does not include all orbitals relevant for the metal-ligand bond, whereas picking the second largest plateau with 14 orbitals (highlighted in blue) would include them.

Reaction 10

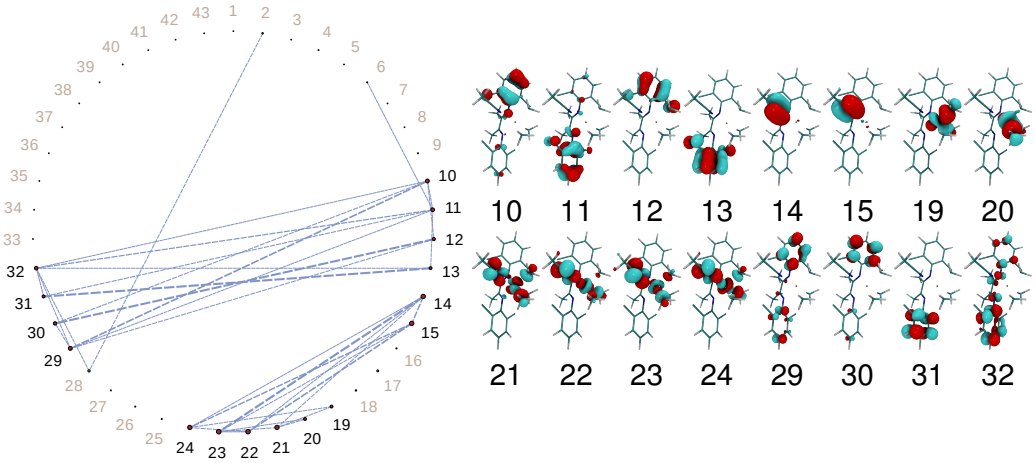

(a) Undissociated complex

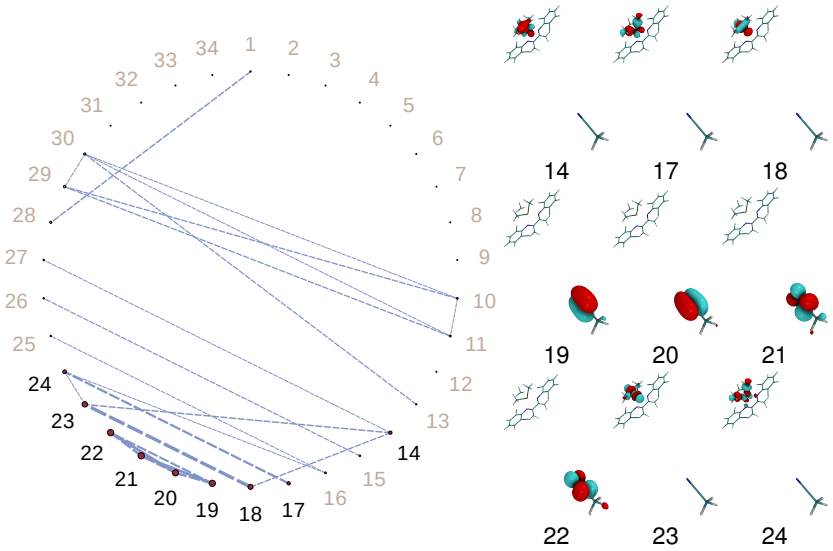

(b) Dissociated complex

Figure 12: Entanglement diagrams calculated from DMRG-CI wave functions for the undissociated (a) and dissociated (b) complex of reaction 10. The area of the red circle is proportional to the single-orbital entropy $s(1)_i$, the blue lines connecting the orbitals show their mutual information value I_{ij}. Solid lines denote I_{ij} values of at least 0.1, dashed lines I_{ij} values of at least 0.01. The automatedly selected orbitals are depicted around the circle and highlighted by black numbers.

Reaction 10 features the dissociation of an acetonitrile ligand which acts

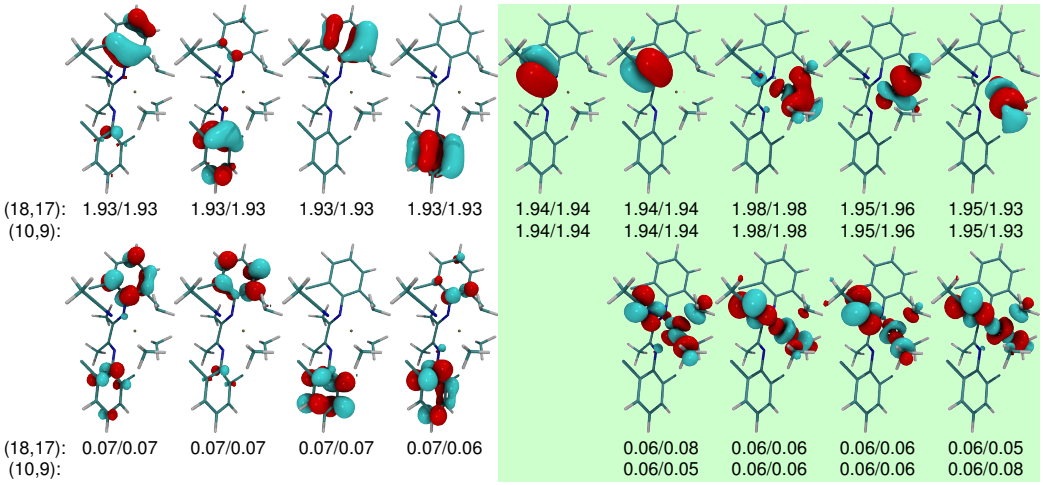

Figure 13: Full CAS(18,17) obtained from the automated selection protocol and reduced CAS(10,9) (highlighted in green), with natural orbital occupation numbers for the undissociated/dissociated complex, respectively.

as a π acceptor. Hence, one would expect static correlation in the metal-acetonitrile bond. Expectantly, the π^* orbitals of acetonitrile interact with the metal d orbitals and show strong entanglement among each other and with the acetonitrile π orbitals (orbitals 14, 15, and 19–24, Figure 12a). A similar entanglement pattern demonstrating static correlation was observed in a metal-nitrosyl bond.[7] Additionally, four π and π^* orbital pairs on the chelating ligand (orbitals 10–13 and 29–32) show strong entanglement. The automatedly selected active space for the undissociated complex comprises 16 electrons in 16 orbitals in total. The dissociated complex shows less entanglement (see Figure 12b). In particular, the π and π^* orbitals of the dissociated acetonitrile ligand do not interact with metal orbitals. However, an additional linear combination of the σ orbitals at the methyl ligands with the metal d orbitals (orbital 14), which was not selected for an active space in the undissociated complex, shows strong entanglement in the dissociated complex, and should be included in the final active space. The resulting final active space consists of 18 electrons in 17 orbitals (see Figure 13).

An active space consisting of 17 orbitals is too large for a CASPT2 calculation. Therefore, we selected a reduced active space consisting of 10 electron in 9 orbitals (see Figure 13, excluding orbitals 10–13 and 29–32 in Figure 12a). The DMRG-SC-NEVPT2(10,9)[256] and DMRG-SC-NEVPT2(10,9)[1024] results (both 100.0 kJ mol^{-1}) are only 1.8 kJ mol^{-1} larger than the DMRG-SC-NEVPT2(18,17)[256] result (98.2 kJ mol^{-1}) (m value is given in square brackets). For consistency, all results presented in

the main paper were obtained with the (10,9) active space.

Summary of Final Active Orbital Spaces

All active spaces which were employed in the multi-reference calculations reported in the main text are summarized in Table 2.

Table 2: Summary of all active spaces denoted as (*no* of electrons, *no* of orbitals) chosen for the multi-reference calculations.

Reaction	CAS	Reaction	CAS
1	(12,12)	6	(12,12)
2	(8,8)	7	(12,12)
3	(8,8)	8	(12,12)
4	(10,10)	9	(14,14)
5	(6,5)	10	(10,9)

2 Multi- and Single-Reference Perturbation Theory

The CASPT2 (IPEA = 0.0 a.u., IPEA = 0.25 a.u.), DMRG-SC-NEVPT2, DMRG-PC-NEVPT2, and MP2/ANO-RCC ligand dissociation energies are presented in Table 3.

Table 3: Ligand dissociation energies calculated with CASPT2 (IPEA = 0.0 a.u., IPEA = 0.25 a.u.), DMRG-SC-NEVPT2, DMRG-PC-NEVPT2, and MP2 and an ANO-RCC basis set in kJ mol^{-1}.

Rct.	CASPT2 IPEA = 0.0 a.u.	CASPT2 IPEA = 0.25 a.u.	DMRG-SC-NEVPT2	DMRG-PC-NEVPT2	MP2/ ANO-RCC
1	93.8	94.2	96.3	96.1	95.3
2	262.8	276.5	273.4	273.3	267.6
3	265.7	275.8	248.7	248.9	269.4
4	183.8	183.9	187.4	189.8	165.5
5	236.8	242.3	254.0	255.2	253.8
6	321.5	324.6	284.1	287.3	321.5
7	299.9	301.1	290.6	291.0	302.8
8	235.3	236.6	229.4	229.8	237.1

Rct.	CASPT2 IPEA = 0.0 a.u.	CASPT2 IPEA = 0.25 a.u.	DMRG-SC-NEVPT2	DMRG-PC-NEVPT2	MP2/ ANO-RCC
9	194.0	193.6	179.7	188.1	216.2
10	108.3	109.3	96.8	98.3	115.6

The CASPT2 (IPEA = 0.0 a.u., IPEA = 0.25 a.u.), DMRG-SC-NEVPT2, DMRG-PC-NEVPT2, and MP2/ANO-RCC electronic energies are presented in Table 4.

Table 4: Electronic energies calculated with CASPT2 (IPEA = 0.0 a.u., IPEA = 0.25 a.u.), DMRG-SC-NEVPT2, DMRG-PC-NEVPT2, and MP2 and an ANO-RCC basis set in Eh.

Rct.	Method	Undissociated	Dissociated
	CASPT2/IPEA=0	-21082.509982	-21082.474273
	CASPT2/IPEA=0.25	-21082.499595	-21082.463707
1	DMRG-SC-NEVPT2	-21082.487688	-21082.451007
	DMRG-PC-NEVPT2	-21082.490052	-21082.453455
	MP2/ANO-RCC	-21082.517858	-21082.481557
	CASPT2/IPEA=0	-3790.535378	-3790.435293
	CASPT2/IPEA=0.25	-3790.529781	-3790.424487
2	DMRG-SC-NEVPT2	-3790.520337	-3790.416203
	DMRG-PC-NEVPT2	-3790.521259	-3790.417184
	MP2/ANO-RCC	-3790.538536	-3790.436596
	CASPT2/IPEA=0	-3790.535378	-3790.434166
	CASPT2/IPEA=0.25	-3790.529781	-3790.424735
3	DMRG-SC-NEVPT2	-3790.520337	-3790.425626
	DMRG-PC-NEVPT2	-3790.521259	-3790.426452
	MP2/ANO-RCC	-3790.538536	-3790.424735
	CASPT2/IPEA=0	-8895.535718	-8895.465696
	CASPT2/IPEA=0.25	-8895.528062	-8895.458020
4	DMRG-SC-NEVPT2	-8896.105948	-8896.014165
	DMRG-PC-NEVPT2	-8896.111291	-8896.018583
	MP2/ANO-RCC	-8895.550447	-8895.487431
	CASPT2/IPEA=0	-39206.398070	-39206.307893
	CASPT2/IPEA=0.25	-39206.395489	-39206.303212
5	DMRG-SC-NEVPT2	-39206.387400	-39206.290676
	DMRG-PC-NEVPT2	-39206.388443	-39206.291239
	MP2/ANO-RCC	-39206.405554	-39206.308868
	CASPT2/IPEA=0	-20105.902856	-20105.780395
6			

Rct.	Method	Undissociated	Dissociated
	CASPT2/IPEA=0.25	-20105.893472	-20105.769848
	DMRG-SC-NEVPT2	-20105.880813	-20105.772623
	DMRG-PC-NEVPT2	-20105.883342	-20105.773912
	MP2/ANO-RCC	-20105.907773	-20105.785326
7	CASPT2/IPEA=0	-2765.638137	-2765.523921
	CASPT2/IPEA=0.25	-2765.628113	-2765.513433
	DMRG-SC-NEVPT2	-2765.627068	-2765.516399
	DMRG-PC-NEVPT2	-2765.628536	-2765.517681
	MP2/ANO-RCC	-2765.643921	-2765.528583
8	CASPT2/IPEA=0	-6424.059456	-6423.969834
	CASPT2/IPEA=0.25	-6424.049501	-6423.959369
	DMRG-SC-NEVPT2	-6424.049616	-6423.962253
	DMRG-PC-NEVPT2	-6424.051076	-6423.963532
	MP2/ANO-RCC	-6424.064956	-6423.974635
9	CASPT2/IPEA=0	-5882.507295	-5882.433421
	CASPT2/IPEA=0.25	-5882.498951	-5882.425225
	DMRG-SC-NEVPT2	-5882.481872	-5882.413443
	DMRG-PC-NEVPT2	-5882.487501	-5882.415862
	MP2/ANO-RCC	-5882.538904	-5882.456543
10	CASPT2/IPEA=0	-21218.378863	-21218.337623
	CASPT2/IPEA=0.25	-21218.374117	-21218.332492
	DMRG-SC-NEVPT2	-21218.364413	-21218.327558
	DMRG-PC-NEVPT2	-21218.366169	-21218.328720
	MP2/ANO-RCC	-21218.400495	-21218.356472

3 Coupled-Cluster Results

In the main text, we presented coupled-cluster (and (SCS-)MP2) results which were extrapolated to the complete basis set limit (CBS). This extrapolation is based on single-point energies obtained with cc-pVTZ(-PP) and cc-pVQZ(-PP) basis sets and follows Ref. 8: The Hartree–Fock energy in the complete basis set limit, $E_{\mathrm{HF}}^{(\mathrm{CBS})}$, is calculated from $E_{\mathrm{HF}}^{(\text{cc-pVQZ})}$ and $E_{\mathrm{HF}}^{(\text{cc-pVTZ})}$,

$$E_{\mathrm{HF}}^{(\mathrm{CBS})} = \frac{e^{-\alpha\sqrt{3}} E_{\mathrm{HF}}^{(\text{cc-pVQZ})} - e^{-\alpha\sqrt{4}} E_{\mathrm{HF}}^{(\text{cc-pVTZ})}}{e^{-\alpha\sqrt{3}} - e^{-\alpha\sqrt{4}}}. \tag{1}$$

An empirical parameter α and the cardinal numbers of the basis sets (3 for cc-pVTZ and 4 for cc-pVQZ) enter this equation. The correlation energy in

the complete basis set limit, $E_{\mathrm{corr}}^{(\mathrm{CBS})}$, is obtained as

$$E_{\mathrm{corr}}^{(\mathrm{CBS})} = \frac{3^{\beta} E_{\mathrm{corr}}^{(\text{cc-pVTZ})} - 4^{\beta} E_{\mathrm{corr}}^{(\text{cc-pVQZ})}}{3^{\beta} - 4^{\beta}}. \quad (2)$$

According to the suggestion in the ORCA Manual, we chose the empirical parameters $\alpha = 5.46$ and $\beta = 3.05$.[9]

The DLPNO-CCSD/cc-pVTZ(-PP), DLPNO-CCSD/cc-pVQZ(-PP), and DLPNO-CCSD/CBS results are presented in Table 5. In the main text, we also compared our results to the ones obtained by Ma *et al.*[10] (Table 5).

Table 5: DLPNO-CCSD and PNO-LCCSD-F12b[10] ligand dissociation energies for BP86/def2-QZVPP optimized structures in kJ mol^{-1}.

Rct.	DLPNO-CCSD/ cc-pVTZ(-PP)	cc-pVQZ(-PP)	CBS	PNO-LCCSD-F12b/ VTZ-F12[a]
1	122.1	111.7	107.6	102.6
2	249.8	242.1	240.7	232.4
3	253.1	242.5	239.6	233.5
4	203.1	202.5	204.3	197.7
5	189.1	179.4	174.8	171.7
6	270.9	271.4	272.7	271.1
7	239.9	237.3	237.4	244.8
8	199.0	198.5	199.3	195.6
9	143.5	140.3	139.0	134.9
10	94.2	92.0	91.6	89.6

[a] Taken from Ref. 10

As stated in the main text, the correlation energy in coupled-cluster calculations is known to converge only slowly with basis-set size. Our DLPNO-CCSD/CBS results deviate on average by 4.8 kJ mol^{-1} from the PNO-LCCSD-F12b/cc-pVTZ-F12 results, but individual deviations may be as large as 8.2 kJ mol^{-1} (reaction 2). While calculations with larger basis sets would certainly be desirable, they are computationally not necessarily feasible.

Our DLPNO-CCSD/cc-pVTZ(-PP) and DLPNO-CCSD/cc-pVQZ(-PP) ligand dissociation energies are summarized in Table 6. In the main text, we also compared our results to the PNO-LCCSD(T)-F12b[11] ones obtained by Werner and co-workers[12] (Table 6).

The DLPNO-CCSD(T) method exploits the locality of correlation effects to accelerate the calculations with respect to canonical CCSD(T).[13,14] The

Table 6: DLPNO-CCSD(T) and PNO-LCCSD(T)-F12b[12] ligand dissociation energies with different basis sets for BP86/def2-QZVPP structures in kJ mol^{-1}.

Rct.	DLPNO-CCSD(T)/			PNO-LCCSD(T)-F12b
	cc-pVTZ(-PP)	cc-pVQZ(-PP)	CBS	VTZ-F12[a]
1	120.8	110.1	105.6	99.7
2	247.9	239.8	238.2	238.2
3	251.4	240.7	237.7	239.3
4	203.5	204.3	207.0	208.1
5	196.9	187.9	183.7	190.1
6	276.0	276.9	278.4	279.3
7	246.8	244.3	244.5	262.3
8	204.6	204.6	205.9	205.3
9	155.1	152.2	151.0	156.1
10	100.0	98.4	98.5	97.8

[a] Taken from Ref. 12

calculations require the specification of certain threshold parameters which ORCA conveniently summarizes into the ready-to-use keywords `LoosePNO`, `NormalPNO`, and `TightPNO` (see Ref. 15 and 9 for a detailed discussion on the definition of these keywords). The `LoosePNO` keyword is only recommended for rapid estimates, the `NormalPNO` setting is the default setting and is recommended for general thermochemistry, and the `TightPNO` setting is required for the accurate determination of conformational equilibria.[15] All results presented in the main text were obtained with the `NormalPNO` setting due to the high computational effort associated with calculating DLPNO-CCSD(T)/cc-pVQZ(-PP) energies with a `TightPNO` setting. A comparison of the DLPNO-CCSD(T)/CBS and the PNO-LCCSD(T)-F12b/VTZ-F12 results highlights critical cases in this respect. We observe deviations of 5.9, 6.3, 18.0, and 5.0 kJ mol^{-1} for reactions 1, 5, 7, and 9, respectively. We applied `TightPNO` settings for reactions 1, 7, and 9 and report the results in Table 7.

Table 8 presents DLPNO-CCSD(T)/cc-pVTZ(-PP) and DLPNO-CCSD(T)/cc-pVQZ(-PP) ligand dissociation energies for BP86-D3(0)/def2-QZVPP structures. The CBS extrapolated energies are given in Table 2 in the main text.

We report the DLPNO-CCSD(T) electronic energies obtained for all BP86 and BP86-D3(0) structures in Table 9.

Table 7: DLPNO-CCSD(T) (TightPNO threshold settings) and PNO-LCCSD(T)-F12b[12] ligand dissociation energies with different basis sets for BP86/def2-QZVPP structures in kJ mol^{-1}.

Reaction	DLPNO-CCSD(T)/ cc-pVTZ(-PP)	DLPNO-CCSD(T)/ cc-pVQZ(-PP)	CBS	PNO-LCCSD(T)-F12b VTZ-F12[a]
1	117.6	106.3	101.5	99.7
7	255.2	251.9	251.4	262.3
10	161.9	157.8	156.0	156.1

[a] Taken from Ref. 20

Table 8: DLPNO-CCSD(T) ligand dissociation energies with different basis sets for BP86-D3(0)/def2-QZVPP structures in kJ mol^{-1}.

Rct.	DLPNO-CCSD(T)/ cc-pVTZ(-PP)	DLPNO-CCSD(T)/ cc-pVQZ(-PP)
1	121.8	111.3
2	277.7	267.9
3	282.1	267.5
4	217.2	216.0
5	200.4	192.3
6	278.7	280.3
7	249.0	248.8
8	207.5	208.4
9	155.3	153.2
10	101.1	99.4

Table 9: DLPNO-CCSD(T) electronic energies obtained with a cc-pVTZ(-PP) or a cc-pVQZ(-PP) basis set for BP86 and BP86-D3(0) optimized structures in Eh. The structures are named according to the number of the reaction (1–10) and an appended letter where 'a' encodes the complex, 'b' the charged fragment, and 'c' the neutral fragment.

Structure	DLPNO-CCSD(T)/ cc-pVTZ(-PP)//		DLPNO-CCSD(T)/ cc-pVQZ(-PP)//	
	BP86	BP86-D3(0)	BP86	BP86-D3(0)
1a	-2799.227606	-2799.227986	-2799.657363	-2799.657976
1b	-2722.849374	-2722.849357	-2723.255830	-2723.255958
1c	-76.332221	-76.332220	-76.359615	-76.359614
2a	-2332.909125	-2332.920841	-2333.637799	-2333.649219

Structure	DLPNO-CCSD(T)/ cc-pVTZ(-PP)//		DLPNO-CCSD(T)/ cc-pVQZ(-PP)//	
	BP86	BP86-D3(0)	BP86	BP86-D3(0)
2b	-1284.502656	-1284.502983	-1284.928453	-1284.928807
2c	-1048.312042	-1048.312072	-1048.618006	-1048.618366
3a	-2332.909335	-2332.921523	-2333.638200	-2333.648801
3b	-1245.257846	-1245.258080	-1245.673052	-1245.673543
3c	-1087.555723	-1087.555991	-1087.873479	-1087.873376
4a	-4458.633957	-4458.642620	-4459.521513	-4459.531051
4b	-3413.142574	-3413.145679	-3413.806531	-3413.810726
4c	-1045.413861	-1045.414214	-1045.637156	-1045.638054
5a	-2067.516299	-2067.518732	-2067.996146	-2067.999296
5b	-1078.554144	-1078.554630	-1078.766968	-1078.767667
5c	-988.887174	-988.887768	-989.157620	-989.158390
6a	-1246.756397	-1246.757558	-1247.176531	-1247.178129
6b	-1057.737371	-1057.737616	-1058.099588	-1058.100026
6c	-188.913886	-188.913790	-188.971466	-188.971356
7a	-1308.403027	-1308.403483	-1308.835261	-1308.836955
7b	-1119.395140	-1119.394870	-1119.770736	-1119.770846
7c	-188.913886	-188.913790	-188.971466	-188.971356
8a	-1258.054967	-1258.056092	-1258.483217	-1258.484840
8b	-1069.063153	-1069.063259	-1069.433806	-1069.434100
8c	-188.913886	-188.913790	-188.971466	-188.971356
9a	-966.965149	-966.965187	-967.310020	-967.310374
9b	-535.312110	-535.312058	-535.465395	-535.465322
9c	-431.593960	-431.593983	-431.786668	-431.786700
10a	-2935.106956	-2935.107673	-2935.571433	-2935.572383
10b	-2802.542453	-2802.542756	-2802.969543	-2802.970122
10c	-132.526401	-132.526406	-132.564412	-132.564415

4 DFT Ligand Dissociation Energies

Tables 10–13 contain the numerical data for the ligand dissociation energies calculated with various (dispersion-corrected) density functionals for BP86/def2-QZVPP optimized structures.

Table 10: Ligand dissociation energies calculated with various GGA and meta-GGA density functionals and a def2-QZVPP basis set in kJ mol^{-1}.

Reaction	BLYP	BP86	PBE	M06-L	TPSS
1	76.8	75.7	81.7	104.5	81.9
2	163.4	166.4	180.9	223.2	175.6
3	164.8	168.2	182.8	226.2	177.6
4	60.5	93.7	110.7	180.9	109.7
5	110.3	132.0	145.8	171.1	146.8
6	237.1	260.0	264.5	249.8	263.2
7	234.6	251.3	256.0	257.5	253.8
8	185.7	202.2	205.7	195.2	202.6
9	106.5	137.7	146.9	146.3	143.4
10	49.2	64.4	73.7	90.1	70.7

Table 11: Ligand dissociation energies calculated with various dispersion-corrected GGA and meta-GGA density functionals and a def2-QZVPP basis set in kJ mol^{-1}.

Reaction	BLYP-D3(BJ)	BP86-D3(BJ)	PBE-D3(BJ)	M06-L-D3(0)	TPSS-D3(BJ)
1	99.6	95.6	93.5	105.7	97.5
2	250.4	253.5	232.4	238.5	243.3
3	252.5	255.8	234.5	241.5	245.7
4	207.5	230.4	187.9	196.0	212.2
5	197.8	215.1	189.4	178.9	206.0
6	261.0	281.7	276.8	253.0	279.3
7	257.1	272.0	268.1	261.1	269.4
8	208.1	222.4	217.2	198.2	217.6
9	147.8	175.8	166.9	149.8	170.3
10	89.6	100.6	94.6	92.7	98.4

Table 12: Ligand dissociation energies calculated with various hybrid and hybrid meta-GGA density functionals and a def2-QZVPP basis set in kJ mol^{-1}.

Reaction	B3LYP	M06-2X	PBE0	TPSSh
1	86.6	117.3	89.0	84.8
2	176.9	225.6	185.3	171.2
3	178.7	228.4	187.5	179.3
4	94.8	188.9	144.8	145.9
5	118.2	151.8	144.8	145.9
6	244.2	237.2	263.8	262.5
7	228.1	220.1	238.6	246.0
8	185.7	181.4	196.9	198.6
9	109.4	129.9	139.9	140.5
10	57.4	79.7	74.9	71.1

Table 13: Ligand dissociation energies calculated with various dispersion-corrected hybrid and hybrid meta-GGA density functionals and a def2-QZVPP basis set in kJ mol^{-1}.

Reaction	B3LYP-D3(BJ)	M06-2X-D3(0)	PBE0-D3(BJ)	TPSSh-D3(BJ)
1	105.3	118.2	100.3	99.9
2	251.2	239.1	239.9	246.2
3	253.5	241.8	241.4	248.6
4	218.6	202.5	210.5	228.0
5	192.4	158.8	189.6	204.8
6	264.4	240.1	276.1	278.3
7	247.3	223.3	250.7	261.5
8	204.7	184.1	208.4	213.4
9	144.3	133.0	160.1	167.1
10	91.1	82.1	95.4	98.1

Tables 14–15 contain the numerical data for the electronic energies calculated with various (dispersion-corrected) density functionals for BP86/def2-QZVPP optimized structures.

Table 14: Electronic energies obtained with various GGA and meta-GGA density functionals and a def2-QZVPP basis set for BP86/def2-QZVPP optimized structures in Eh. The structures are named according to the number of the reaction (1–10) and an appended letter where 'a' encodes the complex, 'b' the charged fragment, and 'c' the neutral fragment.

Structure	BLYP	BP86	PBE	M06-L	TPSS
1a	-2802.890806	-2803.587201	-2801.503618	-2803.184933	-2803.445898
1b	-2726.405252	-2727.083841	-2725.085467	-2726.691596	-2726.941708
1c	-76.456293	-76.474522	-76.387018	-76.453532	-76.472982
2a	-3780.322773	-3781.310758	-3778.163483	-3780.709863	-3781.412513
2b	-2730.042745	-2730.633705	-2728.779188	-2730.165771	-2730.573636
2c	-1050.217790	-1050.613655	-1049.315393	-1050.459081	-1050.771986
3a	-3780.322806	-3781.310836	-3778.163599	-3780.710223	-3781.412614
3b	-2690.734618	-2691.301823	-2689.502204	-2690.835932	-2691.234062
3c	-1089.525411	-1089.944939	-1088.591767	-1089.788127	-1090.110902
4a	-4465.483768	-4467.261253	-4462.828201	-4466.805278	-4467.497659
4b	-3418.416139	-3419.719440	-3416.447284	-3419.333727	-3419.832066
4c	-1047.044569	-1047.506109	-1046.338756	-1047.402656	-1047.623820
5a	-2070.606145	-2071.590368	-2069.670675	-2071.254111	-2071.360444
5b	-1080.104350	-1080.537528	-1079.646966	-1080.337027	-1080.397524
5c	-990.459782	-991.002546	-989.968187	-990.851923	-990.906995
6a	-1249.050817	-1249.711888	-1248.167049	-1249.498185	-1249.721152
6b	-1059.703513	-1060.281935	-1058.979462	-1060.107250	-1060.264158
6c	-189.256992	-189.330934	-189.086858	-189.295777	-189.356733
7a	-2754.000688	-2754.657922	-2752.714045	-2754.198827	-2754.613890
7b	-2564.654342	-2565.231255	-2563.529666	-2564.804964	-2565.160497
7c	-189.256992	-189.330934	-189.086858	-189.295777	-189.356733
8a	-1260.272083	-1260.914378	-1259.371852	-1260.755287	-1260.928687
8b	-1070.944356	-1071.506435	-1070.206654	-1071.385149	-1071.494800
8c	-189.256992	-189.330934	-189.086858	-189.295777	-189.356733
9a	-969.078440	-969.589194	-968.417997	-969.429993	-969.565688
9b	-536.298122	-536.520428	-535.834066	-536.450356	-536.614779
9c	-432.739768	-433.016313	-432.527970	-432.923916	-432.896296
10a	-2938.996307	-2939.777006	-2937.492594	-2939.380604	-2939.679008
10b	-2806.204412	-2806.936996	-2804.819675	-2806.548051	-2806.815894
10c	-132.773172	-132.815479	-132.644853	-132.798255	-132.836172

Table 15: Electronic energies obtained with various hybrid and hybrid meta-GGA density functionals and a def2-QZVPP basis set for BP86/def2-QZVPP optimized structures in Eh. The structures are named according to the number of the reaction (1–10) and an appended letter where 'a' encodes the complex, 'b' the charged fragment, and 'c' the neutral fragment.

Structure	B3LYP	M06-2X	PBE0	TPSSh
1a	-2802.482168	-2802.732833	-2801.628108	-2803.305711
1b	-2726.013381	-2726.252151	-2725.207906	-2726.809012
1c	-76.435799	-76.436022	-76.386292	-76.464399
2a	-3779.677798	-3780.184038	-3778.284647	-3781.142068
2b	-2729.632529	-2729.898539	-2728.838934	-2730.420963
2c	-1049.977884	-1050.199566	-1049.375134	-1050.653611
3a	-3779.677854	-3780.184438	-3778.284769	-3781.142172
3b	-2690.326993	-2690.582882	-2689.554426	-2691.084525
3c	-1089.282806	-1089.514567	-1088.658937	-1089.989365
4a	-4465.026863	-4465.770015	-4463.345792	-4467.249513
4b	-3418.043335	-3418.539908	-3416.798930	-3419.640619
4c	-1046.947423	-1047.158170	-1046.496326	-1047.560794
5a	-2070.425877	-2070.497279	-2069.802580	-2071.246965
5b	-1079.996160	-1079.999605	-1079.701500	-1080.345642
5c	-990.384664	-990.439849	-990.045929	-990.845761
6a	-1248.826799	-1248.974865	-1248.212806	-1249.587413
6b	-1059.521470	-1059.648400	-1059.019044	-1060.154458
6c	-189.212325	-189.236137	-189.093302	-189.332977
7a	-2753.612069	-2753.876343	-2752.796811	-2754.460200
7b	-2564.312850	-2564.556393	-2563.612645	-2565.033530
7c	-189.212325	-189.236137	-189.093302	-189.332977
8a	-1260.067212	-1260.260259	-1259.444877	-1260.805623
8b	-1070.784146	-1070.955049	-1070.276576	-1071.396990
8c	-189.212325	-189.236137	-189.093302	-189.332977
9a	-968.900317	-969.008563	-968.437534	-969.461020
9b	-536.186779	-536.300866	-535.877092	-536.555718
9c	-432.671873	-432.658225	-432.507153	-432.851774
10a	-2938.570923	-2938.865045	-2937.635858	-2939.522418
10b	-2805.810819	-2806.076465	-2804.958177	-2806.675973
10c	-132.738258	-132.758205	-132.649159	-132.819364

Additionally, we calculated closed-shell singlet PBE/def2-QZVPP, open-shell singlet PBE/def2-QZVPP, and open-shell triplet PBE/def2-QZVPP electronic energies. The closed-shell singlet and open-shell singlet results did

not differ. We report the closed-shell singlet and open-shell triplet energies in Table 16.

Table 16: PBE/def2-QZVPP electronic energies for different spin states for BP86/def2-QZVPP optimized structures in Eh. The structures are named according to the number of the reaction (1–10) and an appended letter where 'a' encodes the complex, 'b' the charged fragment, and 'c' the neutral fragment.

Structure	Closed-shell singlet state	Open-shell triplet state
1a	-2801.578299	-2801.504203
1b	-2725.155114	-2725.090636
1c	-76.387362	-76.123374
2a	-3778.304554	-3778.057815
2b	-2728.845808	-2728.734913
2c	-1049.368241	-1048.916176
3a	-3778.304658	-3778.199677
3b	-2689.565024	-2689.453293
3c	-1088.648451	-1088.495579
4a	-4463.122306	-4463.083958
4b	-3416.642485	-3416.596280
4c	-1046.405056	-1046.232313
5a	-2069.791346	-2069.671958
5b	-1079.686063	-1079.550963
5c	-990.032444	-989.863883
6a	-1248.247190	-1248.171288
6b	-1059.048732	-1058.951685
6c	-189.092914	-189.032980
7a	-2752.792040	-2752.728138
7b	-2563.596841	-2563.500525
7c	-189.092914	-189.032980
8a	-1259.450700	-1259.381553
8b	-1070.274934	-1070.148594
8c	-189.092914	-189.032980
9a	-968.473283	-968.387641
9b	-535.864181	-535.723027
9c	-432.545331	-432.473027
10a	-2937.587832	-2929.647378
10b	-2804.903935	-2804.819410
10c	-132.647627	-132.404822

Figures 14 and 15 illustrate the differences of the DFT ligand dissociation energies to the DLPNO-CCSD(T)/CBS results.

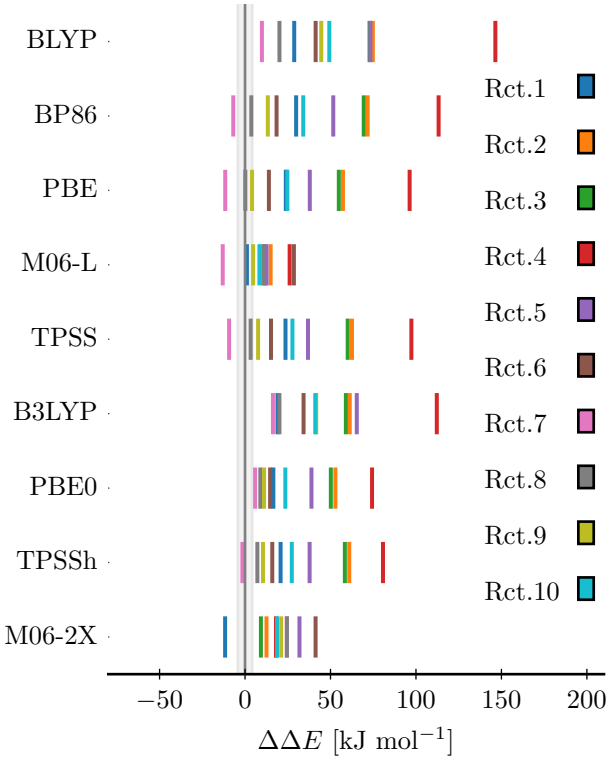

Figure 14: Deviation of pure DFT ligand dissociation energies from DLPNO-CCSD(T)/CBS results ($\Delta\Delta E$) in kJ mol^{-1}. All energies were calculated for BP86/def2-QZVPP optimized structures. The gray region indicates the region where $\Delta\Delta E < 4.2$ kJ mol^{-1}.

We presented dispersion energies which are corrected by Axilrod-Teller-Muto (ATM) corrections in the main text. When including the ATM corrections, the ligand dissociation energies become consistently smaller than when they are omitted. The effect varies between 0.4 kJ mol^{-1} (reaction 6) up to 5.3 kJ mol^{-1} (reactions 2 and 3). This illustrates that ATM corrections are important when the reactants are large.[16]

The D3 dispersion correction must be damped at short interatomic distances to avoid near singularities. The two most popular damping functions are the "zero damping" or Chai–Head-Gordon damping[17] and the Becke–Johnson damping.[18] Generally, the Becke–Johnson damping scheme emerged as the more reliable damping scheme in the recent years.[16] We also see that for most cases, that B3LYP-D3(BJ) more closely reproduces the DLPNO-

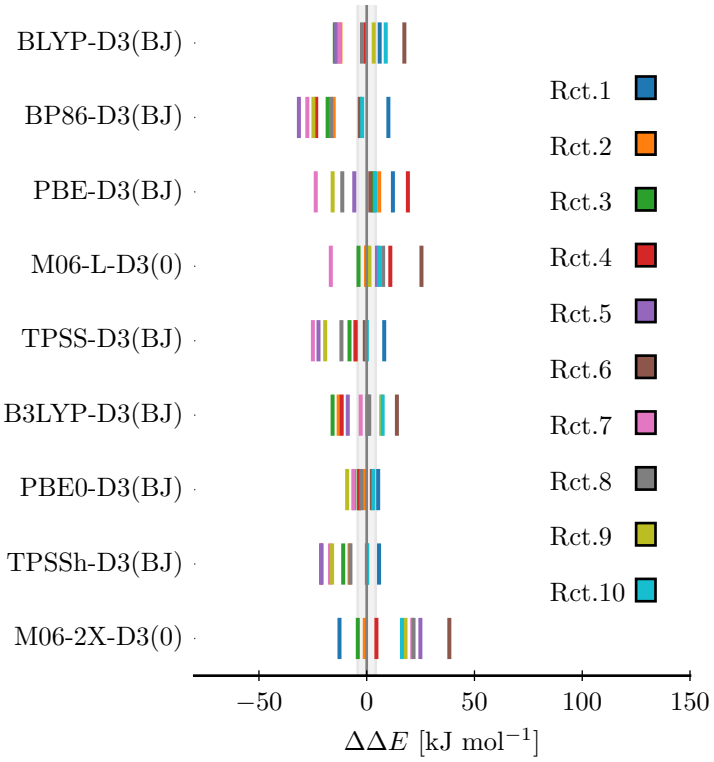

Figure 15: Deviation of dispersion-corrected DFT ligand dissociation energies from DLPNO-CCSD(T)/CBS results ($\Delta\Delta E$) in kJ mol^{-1}. All energies were calculated for BP86/def2-QZVPP optimized structures. The gray region indicates the region where $\Delta\Delta E < 4.2$ kJ mol^{-1}.

CCSD(T) reference than B3LYP-D3(0). The B3LYP-D3(BJ) ligand dissociation energy deviate from the DLPNO-CCSD(T) energies on average by 9.7 kJ mol^{-1}, while the B3LYP-D3(0) ligand dissociation energy deviate on average by 10.2 kJ mol^{-1}. Table 17 contains the mean and largest absolute deviations which were obtained with a zero damping function.

We recently presented the BootD3 program with which the uncertainties of dispersion energies can be estimated.[19] We present the standard deviations obtained from the bootstrapping for the absolute dispersion energies for each molecule and for the relative dispersion energies in Table 18.

In Section 2, we discussed the differences between the DLPNO-CCSD(T) and PNO-LCCSD(T)-F12b results. For four reactions, we reported large differences which can be rationalized with the applied threshold criteria. To assess the effect of the application of the tighter threshold criteria on our conclusions reached in Section 4.3 of the main text, we determined the mean

Table 17: Mean absolute deviations (MAD) and largest absolute deviations (LAD) of ligand dissociation energies calculated with various density functionals with respect to DLPNO-CCSD(T) results in kJ mol^{-1}.

Method	MAD	LAD
PBE-D3(0)	9.9	23.3
BP86-D3(0)	12.6	25.2
BLYP-D3(0)	12.3	24.9
TPSS-D3(0)	9.6	23.9
PBE0-D3(0)	4.9	10.1
B3LYP-D3(0)	10.2	20.9
TPSSh-D3(0)	9.4	19.7

Table 18: Mean and standard deviation of the relative and absolute B3LYP-D3(BJ) dispersion energies in kJ mol^{-1} as obtained from bootstrapping (sample size of 10000).

Rct.	Overall	Reactant	Charged Fragment	Neutral Fragment
1	18.3 ± 1.1	-341.0 ± 16.4	-320.8 ± 16.9	-1.5 ± 0.1
2	77.5 ± 0.9	-605.8 ± 23.5	-297.7 ± 13.6	-233.7 ± 10.7
3	78.1 ± 0.9	-606.2 ± 23.5	-281.5 ± 13.1	-249.1 ± 11.3
4	125.6 ± 4.5	-1260.4 ± 49.6	-848.7 ± 35.0	-288.0 ± 12.3
5	75.4 ± 6.6	-540.8 ± 31.0	-183.3 ± 13.4	-283.3 ± 12.7
6	20.3 ± 1.1	-353.8 ± 14.6	-307.1 ± 12.6	-26.5 ± 1.5
7	19.3 ± 0.8	-342.5 ± 14.0	-296.8 ± 12.2	-26.5 ± 1.5
8	19.0 ± 1.0	-347.3 ± 14.2	-301.8 ± 12.2	-26.5 ± 1.5
9	35.1 ± 2.7	-247.9 ± 11.6	-133.0 ± 6.0	-79.9 ± 4.1
10	33.4 ± 0.7	-427.3 ± 19.1	-381.1 ± 17.9	-12.5 ± 0.7

absolute and largest absolute deviations (MAD and LAD, respectively) of ligand dissociation energies calculated with a selection of density functionals (PBE, BP86, BLYP, TPSS, M06-L, PBE0, B3LYP, TPSSh, and M06-2X) with and without D3 dispersion corrections also with respect to the PNO-LCCSD(T)-F12 results (Table 19).

Table 19: Mean absolute deviations (MAD) and largest absolute deviations (LAD) of ligand dissociation energies calculated with various approximate electronic structure models with respect to DLPNO-CCSD(T) and with respect to PNO-LCCSD(T)-F12b data in kJ mol^{-1}. All DFT calculations were carried out with a def2-QZVPP basis set.

Method	wrt. DLPNO-CCSD(T)		wrt. PNO-LCCSD(T)-F12b	
	MAD	LAD	MAD	LAD
PBE	32.5	96.3	32.8	96.3
BP86	41.2	113.2	42.4	113.2
BLYP	56.1	146.4	58.7	146.4
TPSS	34.4	97.3	35.1	97.3
M06-L	13.2	28.6	14.1	28.6
PBE0	29.7	74.3	32.3	74.3
B3LYP	47.0	112.2	49.6	112.2
TPSSh	32.1	80.7	34.4	80.7
M06-2X	21.4	41.3	25.1	41.3
PBE-D3(BJ)	10.2	23.6	5.8	24.2
BP86-D3(BJ)	17.3	31.5	15.5	33.6
BLYP-D3(BJ)	9.2	17.5	9.1	20.1
TPSS-D3(BJ)	10.6	25.0	8.8	25.5
M06-L-D3(0)	7.7	25.4	7.9	25.0
PBE0-D3(BJ)	4.3	9.1	4.7	9.7
B3LYP-D3(BJ)	8.2	15.8	11.0	21.1
TPSSh-D3(BJ)	10.8	21.1	9.2	25.8
M06-2X-D3(0)	16.3	38.3	19.8	37.9

5 (SCS-)MP2 Ligand Dissociation Energies

Tables 20 and 21 present the MP2 and SCS-MP2 electronic energies and ligand dissociation energies obtained with different basis sets.

Table 20: MP2 and SCS-MP2 ligand dissociation energies for BP86/def2-QZVPP optimized structures in kJ mol^{-1}.

Rct.	MP2/ cc-pVTZ	MP2/ cc-pVQZ	MP2/ CBS	SCS-MP2/ cc-pVTZ	SCS-MP2/ cc-pVQZ	SCS-MP2/ CBS
1	109.3	96.3	90.2	111.5	99.0	93.3
2	263.3	250.7	245.8	246.3	233.4	228.4
3	266.9	252.0	246.1	249.4	234.5	228.6
4	223.8	212.4	206.4	194.5	183.2	177.3
5	253.3	243.2	238.2	221.9	210.7	204.9
6	316.4	316.2	316.9	294.3	293.2	293.3
7	299.6	296.3	295.8	276.2	272.3	271.5
8	238.4	238.2	239.3	218.9	217.7	218.0
9	221.9	218.6	217.2	186.7	182.4	180.4
10	118.5	115.8	115.2	100.6	97.2	96.0

Table 21: Electronic energies obtained with MP2 and SCS-MP2 and various basis sets for BP86/def2-QZVPP optimized structures in Eh. The structures are named according to the number of the reaction (1–10) and an appended letter where 'a' encodes the complex, 'b' the charged fragment, and 'c' the neutral fragment.

Structure	MP2/ cc-pVTZ	MP2/ cc-pVQZ	SCS-MP2/ cc-pVTZ	SCS-MP2/ cc-pVQZ
1a	-2798.976256	-2799.423133	-2798.808136	-2799.281593
1b	-2722.615934	-2723.038940	-2722.449714	-2722.897550
1c	-76.318705	-76.347521	-76.315953	-76.346341
2a	-2332.488705	-2333.272712	-2332.206835	-2333.034902
2b	-1284.339006	-1284.795543	-1284.156146	-1284.635163
2c	-1048.049432	-1048.381696	-1047.956892	-1048.310846
3a	-2332.488395	-2333.272990	-2332.206495	-2333.035170
3b	-1245.110956	-1245.555822	-1244.927906	-1245.394252
3c	-1087.275793	-1087.621179	-1087.183613	-1087.551589
4a	-4457.643557	-4458.603513	-4457.496557	-4458.524113
4b	-3412.453794	-3413.170931	-3412.324254	-3413.090341

Structure	MP2/ cc-pVTZ	MP2/ cc-pVQZ	SCS-MP2/ cc-pVTZ	SCS-MP2/ cc-pVQZ
4c	-1045.104541	-1045.351676	-1045.098241	-1045.363986
5a	-2067.223669	-2067.728406	-2067.091819	-2067.623906
5b	-1078.439844	-1078.661088	-1078.380624	-1078.613538
5c	-988.687354	-988.974690	-988.626664	-988.930120
6a	-1246.474507	-1246.923121	-1246.330587	-1246.805441
6b	-1057.507841	-1057.893498	-1057.373221	-1057.781288
6c	-188.846171	-188.909207	-188.845282	-188.912478
7a	-1308.189817	-1308.656541	-1308.024777	-1308.515971
7b	-1119.229550	-1119.634486	-1119.074280	-1119.499766
7c	-188.846171	-188.909207	-188.845282	-188.912478
8a	-1257.757597	-1258.216067	-1257.615507	-1258.098867
8b	-1068.820613	-1069.216126	-1068.686863	-1069.103476
8c	-188.846171	-188.909207	-188.845282	-188.912478
9a	-966.801979	-967.169950	-966.660659	-967.047210
9b	-535.162580	-535.330795	-535.121890	-535.301715
9c	-431.554900	-431.755908	-431.467670	-431.676018
10a	-2934.809616	-2935.296803	-2934.636866	-2935.153983
10b	-2802.275983	-2802.722423	-2802.113923	-2802.587593
10c	-132.488498	-132.530262	-132.484609	-132.529355

Figure 16 illustrates the differences of MP2/CBS and SCS-MP2/CBS ligand dissociation energies to DLPNO/CBS results.

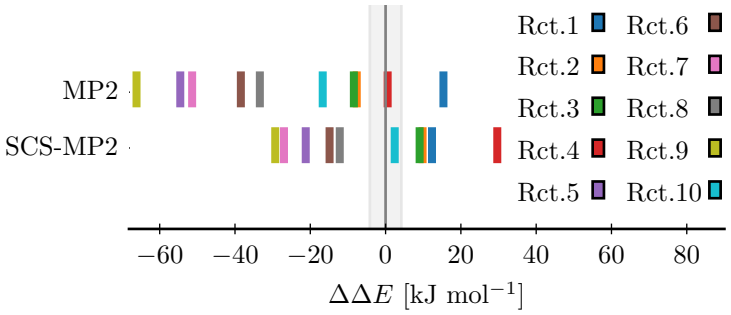

Figure 16: Deviation of MP2/CBS and SCS-MP2/CBS ligand dissociation energies from DLPNO-CCSD(T)/CBS results ($\Delta\Delta E$) in kJ mol^{-1}. All energies were calculated for BP86/def2-QZVPP optimized structures. The gray region indicates the region where $\Delta\Delta E < 4.2$ kJ mol^{-1}.

References

[1] Stein, C. J.; Reiher, M. Automated Selection of Active Orbital Spaces, *J. Chem. Theory Comput.* **2016,** *12,* 1760–1771.

[2] Stein, C. J.; von Burg, V.; Reiher, M. The Delicate Balance of Static and Dynamic Electron Correlation, *J. Chem. Theory Comput.* **2016,** *12,* 3764–3773.

[3] Stein, C. J.; Reiher, M. Automated Identification of Relevant Frontier Orbitals for Chemical Compounds and Processes, *CHIMIA* **2017,** *71,* 170–176.

[4] Legeza, Ö.; Sólyom, J. Optimizing the Density-Matrix Renormalization Group Method Using Quantum Information Entropy, *Phys. Rev. B* **2003,** *68,* 195116.

[5] Rissler, J.; Noack, R. M.; White, S. R. Measuring Orbital Interaction Using Quantum Information Theory, *Chem. Phys.* **2006,** *323,* 519–531.

[6] Stein, C. J.; Reiher, M. Measuring Multi-Configurational Character by Orbital Entanglement, *Mol. Phys.* **2017,** *115,* 2110–2119.

[7] Freitag, L.; Knecht, S.; Keller, S. F.; Delcey, M. G.; Aquilante, F.; Pedersen, T. B.; Lindh, R.; Reiher, M.; González, L. Orbital Entanglement and CASSCF Analysis of the Ru–NO Bond in a Ruthenium Nitrosyl Complex, *Phys. Chem. Chem. Phys.* **2015,** *17,* 14383–14392.

[8] Halkier, A.; Helgaker, T.; Jørgensen, P.; Klopper, W.; Koch, H.; Olsen, J.; Wilson, A. K. Basis-Set Convergence in Correlated Calculations on Ne, N_2, and H_2O, *Chem. Phys. Lett.* **1998,** *286,* 243–252.

[9] orcaforum.cec.mpg.de/OrcaManual.pdf (accessed: 17.10.2017).

[10] Ma, Q.; Schwilk, M.; Köppl, C.; Werner, H.-J. Scalable Electron Correlation Methods. 4. Parallel Explicitly Correlated Local Coupled Cluster with Pair Natural Orbitals (PNO-LCCSD-F12), *J. Chem. Theory Comput.* **2017,** *13,* 4871–4896.

[11] Ma, Q.; Werner, H.-J. Scalable Electron Correlation Methods. 5. Parallel Perturbative Triples Correction for Explicitly Correlated Local Coupled Cluster with Pair Natural Orbitals, *J. Chem. Theory Comput.* **2018,** *14,* 198–215.

[12] Werner, H.-J. , **2018,** private communication.

[13] Riplinger, C.; Neese, F. An Efficient and near Linear Scaling Pair Natural Orbital Based Local Coupled Cluster Method, *J. Chem. Phys.* **2013,** *138,* 034106.

[14] Riplinger, C.; Sandhoefer, B.; Hansen, A.; Neese, F. Natural Triple Excitations in Local Coupled Cluster Calculations with Pair Natural Orbitals, *J. Chem. Phys.* **2013,** *139,* 134101.

[15] Liakos, D. G.; Sparta, M.; Kesharwani, M. K.; Martin, J. M. L.; Neese, F. Exploring the Accuracy Limits of Local Pair Natural Orbital Coupled-Cluster Theory, *J. Chem. Theory Comput.* **2015,** *11,* 1525–1539.

[16] Grimme, S.; Hansen, A.; Brandenburg, J. G.; Bannwarth, C. Dispersion-Corrected Mean-Field Electronic Structure Methods, *Chem. Rev.* **2016,** *116,* 5105–5154.

[17] Grimme, S.; Antony, J.; Ehrlich, S.; Krieg, H. A Consistent and Accurate Ab Initio Parametrization of Density Functional Dispersion Correction (DFT-D) for the 94 Elements H-Pu, *J. Chem. Phys.* **2010,** *132,* 154104.

[18] Grimme, S.; Ehrlich, S.; Goerigk, L. Effect of the Damping Function in Dispersion Corrected Density Functional Theory, *J. Comput. Chem.* **2011,** *32,* 1456–1465.

[19] Weymuth, T.; Proppe, J.; Reiher, M. Statistical Analysis of Semiclassical Dispersion Corrections, **2018,** arXiv:1801.08580.